State-selective electron-capture cross section measurements for low-energy collisions of He-like ions on H_2

G Lubinski, Z Juhász, R Morgenstern and R Hoekstra

KVI Atomic Physics, Rijksuniversiteit Groningen, Zernikelaan 25, 9747 AA Groningen, The Netherlands

Abstract. We measured state-selective absolute electron capture cross sections for collisions of He-like C^{4+}, N^{5+} and O^{6+} ions with molecular hydrogen by means of photon emission spectroscopy at impact energies ranging from 4 keV amu^{-1} down to energies as low as 5 eV amu^{-1}. In this low-energy region the total cross sections are found to be weakly dependent on the projectile energy, whereas the state-selective ones change drastically with varying impact energy. Up to now no experiments were available to benchmark theoretical predictions. In our method we combine for the first time decelerated projectile beams with the possibility of measuring state-selective electron capture.

Compared with existing measurements for state-selective cross sections our deduced cross sections are in perfect agreement in the overlapping energy region ($E \gg 100$ eV amu^{-1}). Good agreement is also found on comparing our results with existing total cross sections. In comparison with theoretical calculations some remarkable and unexpectedly large discrepancies of orders of magnitude are found towards lower impact energies.

1. Introduction

In low-energy collisions between multiply charged ions and neutral targets single-electron transfer dominates in most systems over competing final channels such as excitation, ionization, double capture, etc. One-electron capture in collisions on H_2 can be described by

$$A^{q+} + H_2 \longrightarrow A^{(q-1)+*}(nl) + H_2^+ \longrightarrow A^{(q-1)+}(n'l') + H_2^+ + h\nu \tag{1}$$
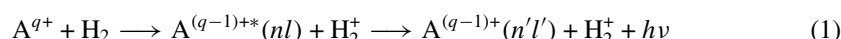
where A represents the projectile ion species with charge state q (in our case O^{6+}, N^{5+} and C^{4+}), n, n' are the principal quantum numbers and l, l' are the angular quantum numbers of the initially populated and the lower state of the radiative transitions, respectively. Single-electron capture has attracted much attention both experimentally and theoretically because of its wide applications in diverse fields of current interest such as diagnostics for magnetically confined fusion plasmas [1, 2], photoionized nebulae [3], or the description of vacuum ultraviolet (VUV) emission from Earth-passing comets such as Hale–Bopp and Hyakutake [4–6], where the cometary emission predominantly takes place on the sunward side [7]. The collision energies one encounters, for example, for the reaction of solar wind ions with neutrals are less than 1 keV amu^{-1}, and the solar wind velocities can be very low during increased solar activity [8]. Up to now in the energy region of $E \ll 1$ keV amu^{-1} there exist hardly any experimental results [9, 10] for state-selective cross sections to benchmark theoretical predictions. So modellers rely completely on theoretical results. While total capture cross sections in this energy region are found to change slowly with impact energy, the situation for the state-selective ones is

predicted to behave differently. In our experiment we combine a low-energy ion beam with the capability of measuring absolute state-selective electron capture cross sections. In this way we are able to obtain the first absolute state-selective electron capture cross sections for O^{6+}, N^{5+} and C^{4+} ions colliding on H_2 at impact energies down to 5 eV amu^{-1}.

There are only a very few theoretical predictions available for the systems under study. For N^{5+} and C^{4+} as projectile ions we can compare our state-selective results with very recent calculations of Kumar and Saha [11], who treated this problem within the framework of the semiclassical close-coupling method using a molecular-orbital (MO) basis expansion for the electronic wavefunctions. Gargaud and McCarroll performed quantum mechanical MO calculations yielding total cross sections for N^{5+} + H_2 and state-selective data for the system C^{4+} + H_2 [12]. For the latter system Errea et al [13] performed ab initio calculations of charge transfer cross sections. For the total cross sections there are in addition recent semiclassical calculations by the same group [14], using the Franck–Condon approximation and a molecular close coupling expansion. In a recalculation they use an improved model potential method [15]. Fritsch [16] uses an atomic-orbital (AO) model for single-electron transfer in slow ion–H_2 collisions within the framework of the semiclassical close-coupling description. His results for C^{4+} projectiles are also compared with our results. On the experimental side our measurements extend up into the energy region ($E \geqslant 1$ keV amu^{-1}) of previous state-selective cross section measurements by Dijkkamp et al [17]. In addition, these authors measured total charge-changing cross sections by means of a retarding-field charge-state analyser. Charge-changing cross sections are also available from the work of Crandall et al [18] and Panov et al [19]. For C^{4+} projectiles, we can directly compare our state-selective results with the earlier ones of Hoekstra et al [20] going down to an impact energy of 50 eV amu^{-1}. For this system Soejima et al [21] also measured charge-changing cross sections.

2. Experimental method

2.1. The crossed-beam set-up

The experiments were performed in a new crossed-beam apparatus at the Atomic-Physics facility at KVI in Groningen. The ions are extracted from an electron cyclotron resonance ion source (ECRIS) with an energy of $3.5q$ keV. After passing several collimating diaphragms, typical beam currents in the collision region are in the range 60–160 nA. Figure 1 gives an artistic impression of the set-up used for the experiments. The highly charged ions A^{q+} are crossed with a gas target (here H_2 molecules) effusing through a liquid-nitrogen-cooled nozzle.

The ions are injected into an octopole ion-beam guide via a system of several electrostatic lenses and diaphragms. During deceleration the whole system consisting of the beam guide, the electrostatic lens system and the diaphragms is connected in series with the high voltage of the ECRIS and a battery. This prevents any shifts in energy due to voltage drifts or instabilities while performing a measurement. The battery shifts the voltage used to decelerate the projectile ions above the primary kinetic energy of the ions (in our experiments a battery voltage of $V_{Batt} = 110$ V was used). In that way we can fully block the ion beam. Setting a voltage V_{Oct} onto the ion beam guide, the energy of the projectile ions E_{Ion} with charge state q can be determined as

$$E_{Ion} = q[(V_{ECR} + V_{Pl}) - (V_{ECR} + V_{Batt} - V_{Oct})]$$

$$= q[(V_{Oct} - (V_{Batt} - V_{Pl})] \tag{2}$$

with $q(V_{ECR} + V_{Pl})$ being the energy of the ions extracted from the ECRIS, V_{Pl} the plasma
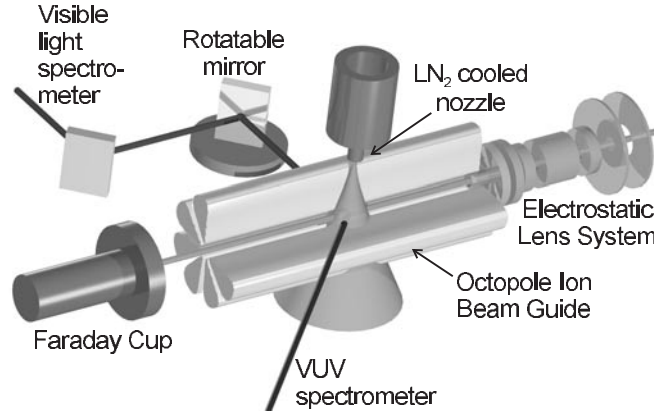
Figure 1. Schematic view of the experimental set-up.

potential of the source and V_{Batt} the battery voltage.

While decelerating the ions down to some eV amu^{-1} the beam current measured in a Faraday cup at the end of our set-up did not decrease over the whole range of the projectile energies. Figure 2 shows the measured ion beam current of a N^{5+} projectile beam with an initial energy of 17.5 keV as a function of the applied DC voltage on the octopole (V_{Oct}) (figure 2(a)). From the derivative of the obtained curve (figure 2(b)) we find, in this case, a plasma potential of 15.7 V and an energy spread of the primary ion beam of 4.2 V. For N^{5+} ions this translates to an energy spread ~ 1.5 eV amu^{-1}. This sets the lower limit to ~ 5 eV amu^{-1}. In combination with an ion source from which ions are extracted with smaller energy spreads, experiments can be performed at lower energies. As such a source, a recoil ion source might be considered which can produce cold ions (~ 0.1 eV amu^{-1} [22]). Since the minimum and maximum values measured are between 12 and 20 V, we have included a plasma potential of 16 V with an uncertainty of 4 V in the analysis of all our measurements.

The technique of RF ion beam guiding was pioneered by Teloy and Gerlich [23] (for a review see [24]) for singly charged ions. Okuno et al [25] introduced an octopole ion beam guide in the field of highly charged ion physics. The divergence of the decelerated ion beam is prevented by supplying an additional radio-frequency (RF) voltage to the octopole with a phase difference of 180° between neighbouring poles. The effective potential V_{eff} an ion with mass m and charge state q experiences at a position r in a multipole ion beam guide with $2N$ poles is given by

$$V_{eff}(r) = \frac{(N q V_{RF})^2}{4m(\omega r_0)^2} \left(\frac{r}{r_0} \right)^{2(N-1)} \tag{3}$$

where V_{RF} is the applied RF voltage with frequency ω (typically in the range 12–25 MHz) and r_0 is the inner radius of the beam guide. To confine an ion with an energy E_m in the guide one has to satisfy the following stability criteria for the minimum RF voltage V_{min} and minimum frequency ω_{min} on the octopole [24]:

$$V_{min} = 8 \frac{N-1}{N} \frac{E_m}{q \eta_m r_m^N} \tag{4}$$

$$\omega_{min} = \frac{1}{2\pi} \sqrt{\frac{16(N-1)^2 E_m}{m(\eta_m r_0 r_m)^2}}. \tag{5}$$
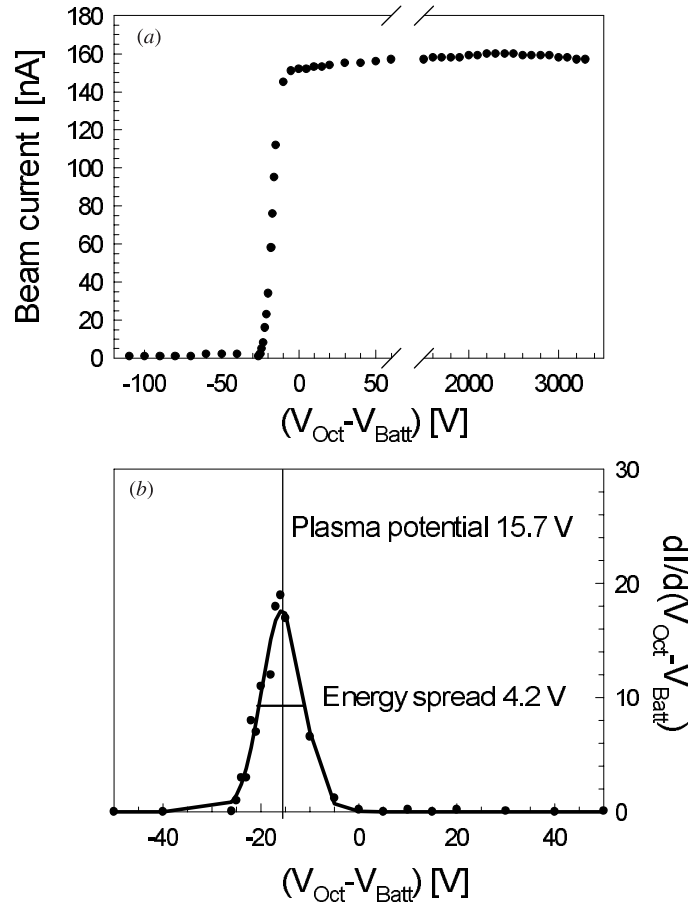
Figure 2. Measured ion beam current as a function of the ion's energy while decelerating the N^{5+} projectiles. The initial energy of the beam was 17.5 keV, the battery voltage 110 V. (a) shows the measured beam current, (b) the first derivative of the current yielding the plasma potential and the energy spread of the initial beam.

Here r_m is the maximum relative amplitude of the ion's motion and η_m is the maximum tolerable value of the so-called adiabacity parameter η [23, 24]. The determination of $\eta_m = 0.3$ is based on numerical simulations and experimental observations [24].

Our choice for an octopole ion beam guide is a compromise between a steep potential ($\propto r^6$) with a large flat interior and the visibility of the ion beam in between the elements to allow for photon emission spectroscopy. Our beam guide consists of eight elements with a length of 100 mm inscribed on a circle of 5.5 mm. The new design of the octopole in comparison to our first attempt with rods of 1 mm diameter [26] provides better handling, higher rigidity and a reduction of DC field penetration from outside the octopole (grounded vacuum chamber). Figure 3 shows a computer-simulated contour map of the new octopole [27]. Here a DC voltage of 3500 V was put on the eight elements and the octopole was directly surrounded by a grounded cylinder representing a worst-case scenario. The plotted lines are equipotential lines illustrating the penetration of the ground potential through the octopole elements. The deviation from the set voltage compared with the voltage in the centre of the octopole is of the order of some millivolts. The actual voltage an ion beam
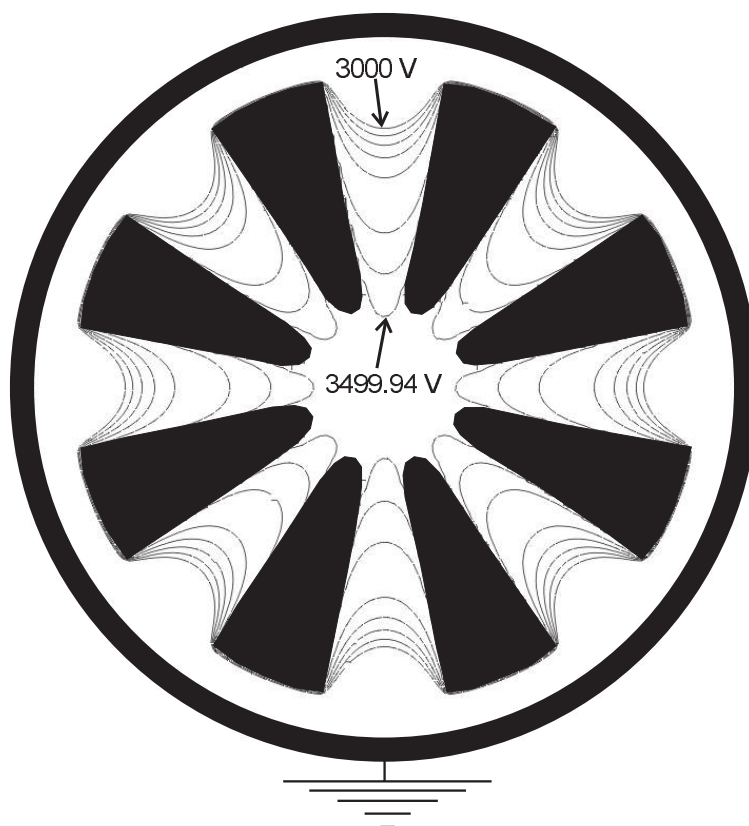
Figure 3. Computer-simulated contour map of the static voltages on the octopole ion beam guide [27]. The plotted curves representing equipotential lines show the penetration of the ground potential (surrounding cylinder) through the elements of the octopole, which were set at a DC voltage of $V_{Oct} = 3500$ V. Arbitrary potential lines between 3000 and 3499.94 V are shown (going inwards).

experiences in the centre of the octopole ion beam guide is thus equal to the DC voltage set on the elements. The ion's energy is therefore defined by the DC voltage set onto the octopole (see equation (2)).

2.2. The photon detection system

2.2.1. Absolute calibration of the VUV spectrometer. During the collision of the highly charged projectile ion with the target molecule, electrons are quasi-resonantly captured into excited states of the ion. The resulting photon emission is observed by a vacuum-ultraviolet (VUV) spectrometer. A position-sensitive microchannel plate detector enables simultaneous detection of lines within a window of 18 nm with the chosen grating (600 lines/mm) and angle of incidence (86°). The spectrometer covers a spectral range from 4.6 nm up to 84 nm.

The absolute emission cross section $\sigma_{em}(\lambda)$ can be determined from the measured signal $S(\lambda)$ via

$$\sigma_{em}(\lambda) = \frac{4\pi}{\Omega} F(v, \tau) P \frac{qe}{QK(\lambda)} \frac{S(\lambda) B_V^{-1}}{\int_L n(z)\, dz} \tag{6}$$

where Ω is the solid angle of observation, $F(v, \tau)$ is a correction factor in the case where the lifetime τ of the decaying state is so long that a considerable fraction of the ions decays outside the observation range of the spectrometer, P is a correction factor for the polarization of the emitted photons, q is the charge state of the projectile ions, e is the electronic charge, Q is the accumulated ion charge, $K(\lambda)$ is the quantum efficiency of the detector, $n(z)$ is the target density at a position z along the beam axis, L is the observation length of the spectrometer and B_V is the visibility of the interaction region along the beam axis (see section 2.2.2). The overall sensitivity

$$K'(\lambda) = \frac{\Omega}{4\pi} n_t K(\lambda) \tag{7}$$

of the VUV spectrometer, where n_t is the effective target density given by

$$n_t = \int_L n(z)\,dz \tag{8}$$

is calibrated with respect to the wavelength of the diffracted photons by observing photon emission for collision systems with well known electron capture cross sections [28]. For all capture processes studied in this paper the factor $F(v, \tau)$ is equal to 1 due to the fast subsequent decay of the excited states formed. Furthermore, the spectrometer is positioned under $54.7°$ with respect to the ion beam axis and tilted by $45°$ to cancel polarization effects [28], i.e. P is equal to 1. Now formula (6) can be reduced to

$$\sigma_{em}(\lambda) = \frac{qe}{Q} \frac{S(\lambda) B_V^{-1}}{K'(\lambda)}. \tag{9}$$

We used the well known He II $(2p \to 1s)$ emission cross sections for $He^{2+} \longrightarrow H_2$ collisions [29] and the undecelerated C^{4+}, N^{5+} and O^{6+} ion beams as calibration measurements which are repeated several times in between the absolute cross section measurements with the decelerated ion beams enabling us to correct, for example, for small fluctuations in target density.

2.2.2. Viewing area of the spectrometer.
The last two apertures (both 1 mm diameter and 4 mm apart) positioned directly in front of the octopole together with diaphragms upstream of the ion beam limit the divergence angle to $1.1°$. This enables us—in case of an undecelerated projectile beam—to fully observe the whole interaction region since the window in between the elements through which we do photon spectroscopy is 1.3 mm in height. For the observation of decelerated ions the situation differs slightly due to the relative enhancement of the radial motion of the ions s. Without superimposing the RF voltage on the octopole, the interaction region is no longer completely viewed by the spectrometer. The reason is that the applied DC voltage for decelerating the projectiles acts only on the longitudinal component of the ion velocity, whereas the radial component remains basically unchanged. This causes the ion beam to diverge while being decelerated. The visibility of the beam is expressed by the factor B_V in equation (6). When the RF voltage on the octopole is high enough to compensate the radial spreading of the beam, the overlap of the beam and target is fully viewed by the spectrometer and the visibility is then 100%. In figure 4 one can observe the behaviour of the apparent absolute capture cross section $\sigma_{ap} = B_V \sigma_{em}$ for a N^{5+} projectile beam with an energy of 25 eV amu^{-1}, while changing the RF voltage on the octopole (here given by the voltage readout of the RF amplifier). The value for the measured cross section saturates at a certain applied octopole voltage. We always operated the octopole at a voltage (indicated by the vertical lines in the figure) far above the starting point of the saturation, thereby ensuring
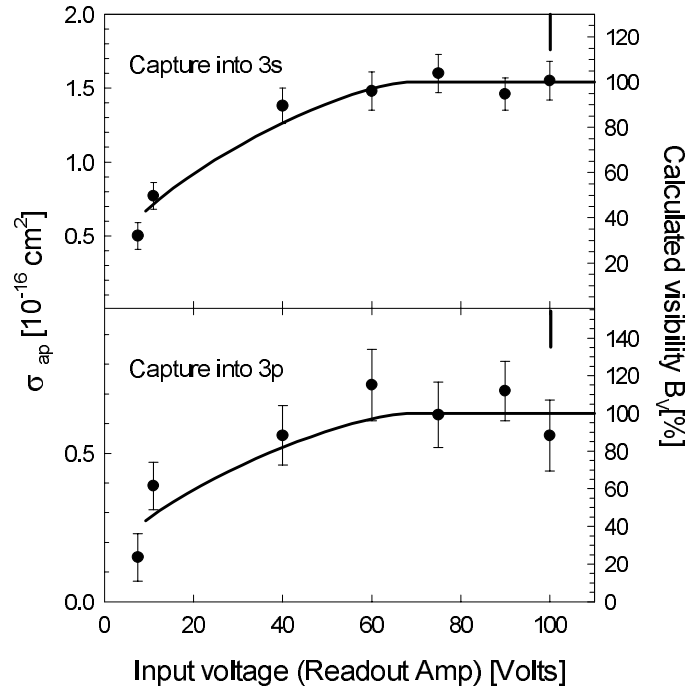
Figure 4. Apparent absolute capture cross sections σ_{ap} as a function of the amplitude of the applied RF voltage on the octopole ion beam guide at a frequency of 14 MHz. σ_{ap} are shown for the 3s $\rightarrow$ 2p and 3p $\rightarrow$ 2s emission lines of N^{5+} colliding on H_2 at an impact energy of 25 eV amu^{-1}, $\bullet$. The full curve shows a calculation of the visibility B_V. We set the maximum value of σ_{ap} reached to 100% visibility. The error bars represent a sum of the statistical error at 90% confidence level. The vertical lines at the upper abscissae give the value of the voltage the octopole was operated at in all presented experiments.

100% visibility. Figure 4 also contains a calculation we performed concerning the visibility B_V of a decelerated N^{5+}-ion beam with an energy of 25 eV amu^{-1} and a beam current of 130 nA. Here we calculate the equilibrium radius of the beam, i.e. the radius for which the RF voltage on the octopole balances the space-charge fields of the projectile ions.

2.2.3. Inßuence of the ionÕs trajectory on the measured photon signal. Since the ion starts to oscillate in the octopole when being decelerated the path length of the ion through the observation window will increase in comparison with that of the calibration measurement (straight line trajectories). The determination of the absolute cross section from the photon signal of the decelerated ion beam may lead to an overestimated cross section because of the underestimated path length. At the lowest ion energies in the octopole the N^{5+} ions are typically injected into the octopole with an energy $E \approx 2$ keV, determined by the voltage on the last collimating diaphragm. Together with the acceptance angle of $1.1°$ this results in a maximum perpendicular energy of $E_{\perp,\max} = E \sin^2 1.1° = 0.74$ eV. Comparing the respective velocities this leads to a ratio $v_\perp/v = 0.09$ at the lowest measured impact energies 7 eV amu^{-1}, resulting in an overestimation of the cross section by 9%. This is a worst-case scenario because the equilibrium between RF and space-charge fields tends to reduce the beam divergence.
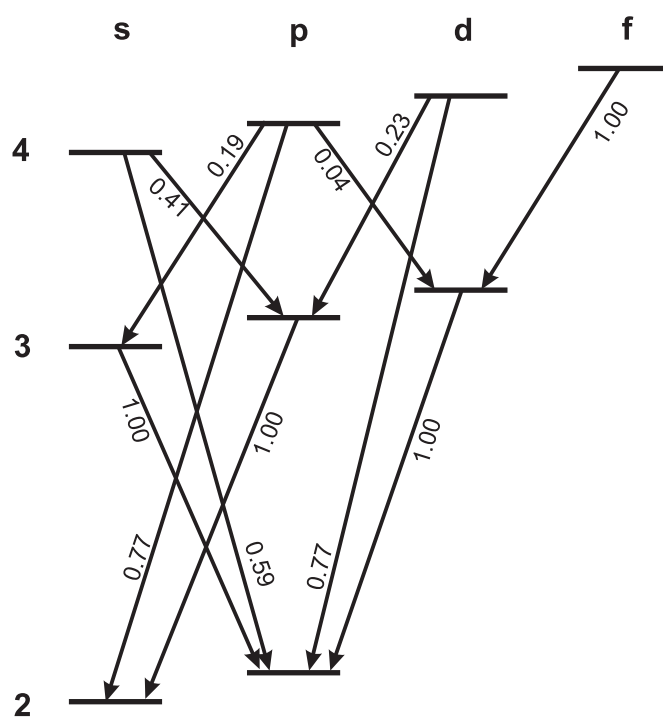
Figure 5. Decay scheme of lithium-like ions. Branching ratios for N v and O vi are indicated [31]. Together with the slightly different C iv ones they are given in table 1.

Table 1. Wavelengths for all observed dipole transitions together with the respective branching ratios (in brackets).

	Ion					
	C^{4+}		N^{5+}		O^{6+}	
Transition	λ (nm)		λ (nm)		λ (nm)	
2s–3p	31.2	(0.99)	20.9	(1.00)	15.0	(1.00)
2p–3s	42.0	(1.00)	26.6	(1.00)	18.4	(1.00)
2p–3d	38.4	(1.00)	24.8	(1.00)	17.3	(1.00)
2s–4p	24.5	(0.78)	16.3	(0.77)	11.6	(0.77)
2p–4s	29.7	(0.59)	19.0	(0.59)	13.2	(0.59)
2p–4d	28.9	(0.77)	18.6	(0.77)	13.0	(0.77)
3s–4p	—		—		44.8	(0.19)
3p–4s	—		—		53.6	(0.41)
3p–4d	—		—		49.8	(0.23)
3d–4f	—		—		52.0	(1.00)

2.3. Analysis of optical data

Figure 5 shows the relevant part of the Grotrian diagram [30] of lithium-like ions including the branching ratios for all dipole transitions [31]. The experimentally observed transitions and their respective wavelengths for C iv, N v and O vi are given in table 1. As an example figure 6 shows two typical spectra for N^{5+} ions colliding on H_2 obtained at different impact energies. After background subtraction the peak integrals give the intensities for the respective
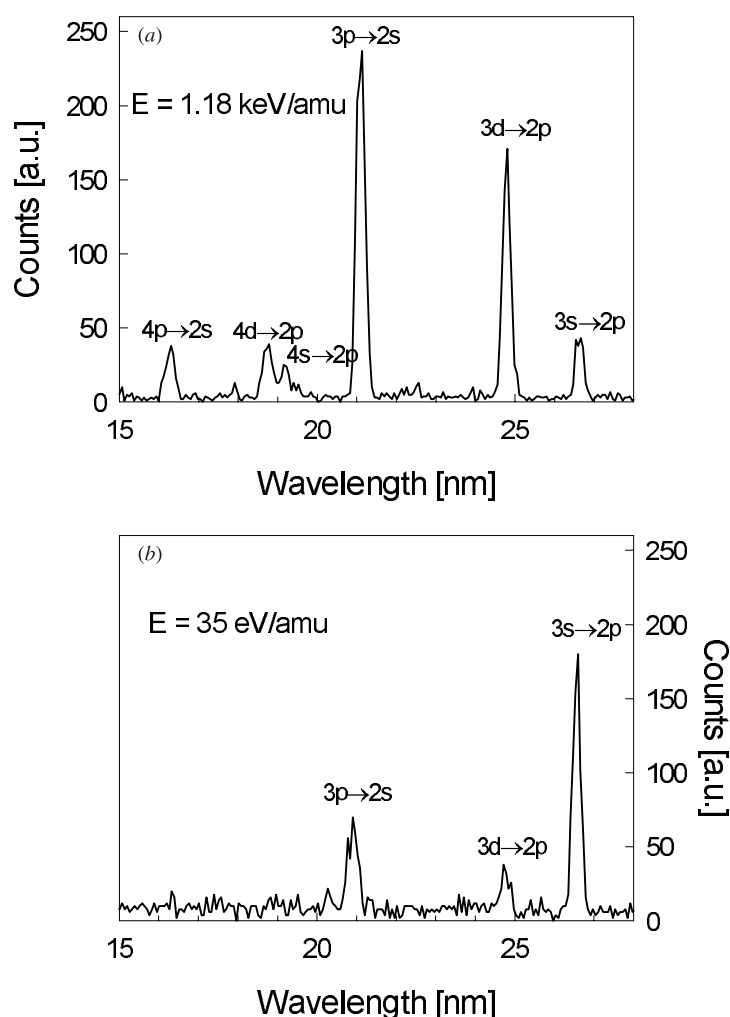
Figure 6. Typical spectra for N^{5+} colliding on H_2 for two projectile energies. For each peak the corresponding transition is indicated.

wavelengths, which can be directly converted into emission cross sections. For C^{4+} and N^{5+} projectile ions, the measured emission cross sections do not need to be corrected for cascades from higher n-levels to obtain capture cross sections since capture predominantly takes place into the $n = 3$ shells. Dijkkamp et al showed that even at higher projectile energies the $n = 4$ compared with the $n = 3$ capture cross sections are still one order of magnitude smaller and that they decrease with decreasing impact energy [17]. Nevertheless, we kept track of the populations of the $4l$ levels by observing the $4l \rightarrow 2l'$ ($l = s, p, d$) transitions. Since these transitions have larger branching ratios than the $4l \rightarrow 3l'$ ones (cf figure 5) and the observed photon signals stemming from these transitions are found to be smaller by two orders of magnitude or more compared with the signals of the $3l \rightarrow 2l'$ ones, cascades from the $n = 4$ states can be neglected. For O^{6+} projectiles the measured emission lines out of the $n = 3$ levels have to be corrected for cascades out of the predominantly populated $n = 4$ levels [17] using

the following formulae:

$$\sigma_{4s} = \sigma_{em}(53.6)/0.41 \tag{10}$$

$$\sigma_{4p} = \sigma_{em}(11.6)/0.77 \tag{11}$$

$$\sigma_{4d} = \sigma_{em}(49.8)/0.23 \tag{12}$$

$$\sigma_{4f} = \sigma_{em}^c(52.0) \tag{13}$$

$$\sigma_{3s} = \sigma_{em}(18.4) - 0.19\sigma_{cap}(4p)$$
$$= \sigma_{em}(18.4) - 0.19(\sigma_{em}(11.6)/0.77) \tag{14}$$

$$\sigma_{3p} = \sigma_{em}(15.0) - \sigma_{em}(53.6) - \sigma_{em}(49.8) \tag{15}$$

$$\sigma_{3d} = \sigma_{em}(17.3) - \sigma_{em}(52.0) - 0.04\sigma_{cap}(4p)$$
$$= \sigma_{em}(17.3) - \sigma_{em}(52.0) - 0.04(\sigma_{em}(11.6)/0.77). \tag{16}$$

The signal for the emission line at 52 nm was corrected for contributions of the third-order 2p–3d and the fourth-order 2p–4d transitions comparing higher-order peaks at other wavelengths with their first-order signals in the following way:

$$S^c = S(52.0) - \frac{S(55.2)}{S(18.4)}S(17.3) - \frac{S(46.4)}{S(11.4)}S(49.8)0.77/0.23$$

leading to

$$\sigma_{em}^c(52.0) = \frac{qe}{Q}\frac{S^c(52.0)B_V^{-1}}{K'(52.0)}.$$

3. Experimental results and discussion

The experimental results are given in tables 2–4 and shown in figures 7–11. The relative errors given in the tables and included in the graphs represent the quadratic sums of the statistical errors at a 90% confidence level and target density uncertainties, which are due to possible fluctuations in the target density and the overlap of the ion and target beams.

Table 2. Absolute state-selective electron capture cross section for C^{4+} colliding on H_2. The errors represent relative errors only. The systematic absolute uncertainty is 20%.

E (eV amu^{-1})	3s (10^{-16} cm^2)	3p (10^{-16} cm^2)	3d (10^{-16} cm^2)
5	8.4 ± 1.1	35.1 ± 1.9	1.8 ± 0.8
10	10.7 ± 1.1	37.8 ± 2.0	1.9 ± 0.8
15	12.5 ± 1.4	41.6 ± 2.2	2.3 ± 1.0
25	11.7 ± 1.1	32.0 ± 1.7	1.9 ± 0.7
48	13.7 ± 1.1	30.1 ± 1.6	2.0 ± 0.7
70	16.0 ± 1.1	24.4 ± 1.3	2.1 ± 0.7
100	14.3 ± 1.0	19.6 ± 1.1	1.5 ± 0.5
200	20.5 ± 1.2	21.0 ± 1.1	1.9 ± 0.5
300	19.3 ± 1.2	16.7 ± 0.9	3.4 ± 0.5
400	18.7 ± 1.1	13.3 ± 0.8	3.9 ± 0.5
600	20.7 ± 1.2	9.7 ± 0.7	5.1 ± 0.6
830	16.5 ± 1.0	7.5 ± 0.5	4.9 ± 0.5
1167	15.9 ± 1.4	7.1 ± 0.6	4.7 ± 0.6

Table 3. Measured capture cross section for $N^{5+} + H_2$ collisions. The errors represent relative errors only. The systematic absolute uncertainty is 20%.

E (eV amu^{-1})	3s (10^{-16} cm^2)	3p (10^{-16} cm^2)	3d (10^{-16} cm^2)
7	2.0 ± 0.2	0.4 ± 0.2	0.4 ± 0.2
10	2.4 ± 0.2	0.5 ± 0.2	0.4 ± 0.2
16	1.7 ± 0.1	0.6 ± 0.1	0.4 ± 0.1
21	1.2 ± 0.1	0.6 ± 0.1	0.3 ± 0.1
26	1.3 ± 0.1	0.8 ± 0.1	0.2 ± 0.1
38	1.6 ± 0.1	0.9 ± 0.1	0.4 ± 0.1
56	1.7 ± 0.1	1.0 ± 0.1	0.4 ± 0.1
84	1.6 ± 0.1	1.3 ± 0.1	0.5 ± 0.1
101	1.0 ± 0.1	1.1 ± 0.1	0.4 ± 0.1
156	0.8 ± 0.1	1.1 ± 0.1	0.6 ± 0.1
216	0.4 ± 0.1	0.5 ± 0.1	0.6 ± 0.1
307	0.4 ± 0.1	0.5 ± 0.1	0.9 ± 0.1
400	0.4 ± 0.1	0.9 ± 0.1	1.2 ± 0.1
600	0.5 ± 0.2	1.4 ± 0.2	2.0 ± 0.2
700	0.7 ± 0.2	2.1 ± 0.3	2.8 ± 0.3
929	0.8 ± 0.2	3.0 ± 0.2	3.4 ± 0.2
1000	0.7 ± 0.1	3.3 ± 0.2	3.1 ± 0.2
1190	1.0 ± 0.1	4.2 ± 0.2	3.4 ± 0.2
2000	1.4 ± 0.2	6.4 ± 0.3	3.6 ± 0.2
4000	1.9 ± 0.2	6.0 ± 0.3	5.6 ± 0.3

Table 4. Measured one-electron capture cross sections for the system $O^{6+} + H_2$. The errors represent relative errors only. The systematic absolute uncertainty is 20%.

E (eV amu^{-1})	4s (10^{-16} cm^2)	4p (10^{-16} cm^2)	4d (10^{-16} cm^2)	4f (10^{-16} cm^2)
7	2.4 ± 1.3	17.9 ± 2.5	0.4 ± 0.4	0.2 ± 0.2
15	2.5 ± 1.2	21.7 ± 2.8	0.6 ± 0.4	0.2 ± 0.2
20	3.7 ± 1.1	25.2 ± 2.5	0.7 ± 0.3	0.3 ± 0.1
32	4.0 ± 1.7	32.4 ± 2.4	0.8 ± 0.5	0.4 ± 0.3
50	5.6 ± 1.6	31.8 ± 2.6	1.0 ± 0.5	1.1 ± 0.6
70	8.7 ± 2.7	31.7 ± 2.4	1.3 ± 0.5	2.4 ± 1.1
100	9.8 ± 1.7	27.8 ± 2.3	1.5 ± 0.5	3.9 ± 1.4
150	11.7 ± 2.1	21.6 ± 2.0	2.2 ± 0.5	4.0 ± 2.0
250	13.9 ± 1.9	15.0 ± 2.1	2.8 ± 0.4	5.9 ± 1.1
350	12.3 ± 2.2	13.9 ± 1.8	3.1 ± 0.7	6.7 ± 1.5
560	14.3 ± 2.1	10.7 ± 1.8	3.1 ± 0.6	5.8 ± 1.3
750	12.3 ± 1.6	9.2 ± 1.7	3.2 ± 0.6	8.0 ± 1.6
980	9.4 ± 1.7	7.9 ± 1.7	3.0 ± 0.5	7.9 ± 1.6
1313	10.0 ± 2.1	8.4 ± 1.8	4.2 ± 0.6	6.5 ± 1.1

To estimate the uncertainties of the target density we compared the photon signals of the calibration measurements. The variation of these signals was observed to be not more than 5% over a whole day of measurements. Apart from the relative errors there is a systematic uncertainty of 20% for all the results due to the overall absolute calibration of the VUV spectrometer.

Another contribution to the systematic error might be the role of the metastable fraction in the primary ion beam. The flight times of all studied ions from the source to the set-up are approximately 18 μs. Table 5 gives the lifetimes and experimentally determined fractions
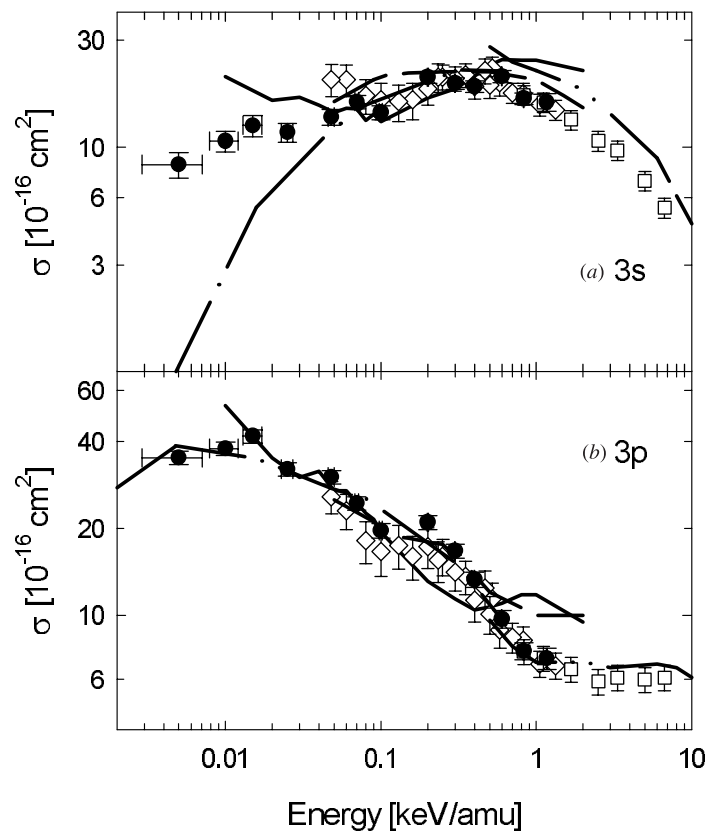
Figure 7. Absolute capture cross sections for C^{4+} ions colliding on H_2 for capture into the respective l-substates (a)–(c) and for total capture (d). Theoretical calculations: — · —, Gargaud and McCarroll [12]; ——, Kumar and Saha [11]; – – –, Errea et al [13]; — · · —, Fritsch [16]. Experiments: □, Dijkkamp et al [17]; ◇, Hoekstra et al [20]; ▽, Panov et al [19]; △, Crandall et al [18]; ○, Soejima et al [21]; ●, this work.

Table 5. Lifetimes and fractions of metastable states for the projectile ions used.

Ion	Metastable state	Lifetime [41]	Fraction (%)
C^{4+}	$(1s2s)^1S$	$3.0 \, \mu s$	—
	$(1s2s)^3S$	$112 \, s$	5 ± 2 [42]
N^{5+}	$(1s2s)^1S$	$1.1 \, \mu s$	—
	$(1s2s)^3S$	$18 \, s$	8 ± 3 [42]
O^{6+}	$(1s2s)^1S$	$0.4 \, \mu s$	—
	$(1s2s)^3S$	$4 \, s$	2.6 ± 0.5 [43]

of metastable states of interest in this work (for review articles see, e.g., [32–35]). This is in general agreement with the findings of Mack [36], who gives a value of $(5 \pm 3)\%$ for the fraction of metastables in all He-like ion beams. Since in all cases the fraction of metastable states is of the order of only a few per cent with a high uncertainty we do not correct for metastable states in our results. The fraction of metastables hardly has any influence when using undecelerated projectile beams of C^{4+}, N^{5+} and O^{6+} as a calibration measurement.
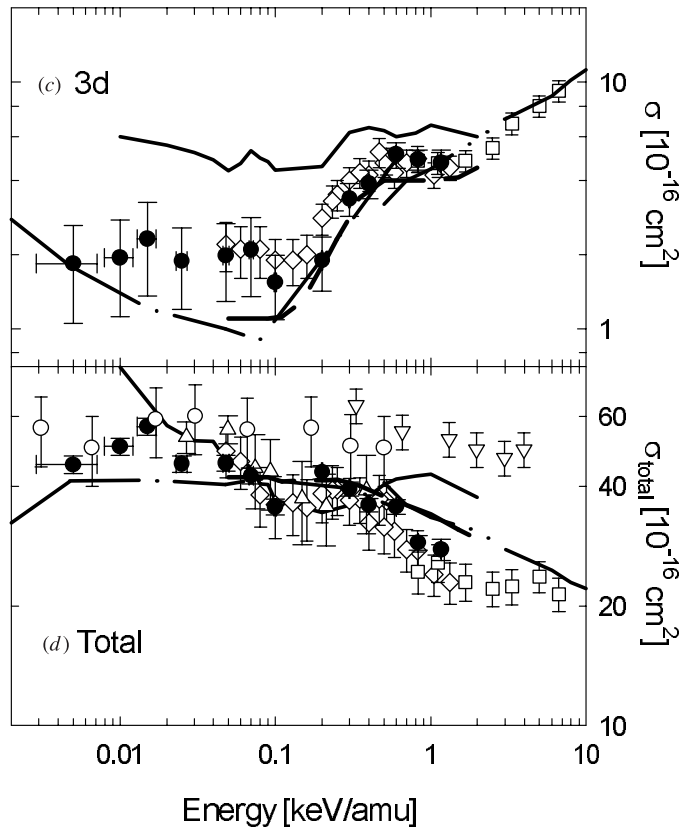
Figure 7. Continued.

The uncertainty in the determination of the ion energy as shown in the figures stems from the uncertainties in the plasma potential V_{Pl} (4 V), the octopole voltage V_{Oct} (1 V) and the battery voltage V_{Batt} (0.5 V).

3.1. General comparison of the presented data with other experimental results

All state-selective cross sections obtained for the systems C^{4+}, N^{5+} and O^{6+} on H_2 agree excellently with other experimental results available in the overlapping impact energy region. Comparing our summed partial cross sections with charge-changing $(q \rightarrow q-1)$ cross sections, we find good agreement in the case of $C^{4+} + H_2$. The only exceptions to that fact are the measurements at somewhat higher projectile energies by Panov et al [19], but their results also differ from those by Crandall et al [18] and Dijkkamp et al [17]. The remarkably good match with the latter two is not a strict necessity, since the charge-changing cross sections can include contributions from double-electron capture into autoionizing states (ADC). Our results indicate that these contributions are negligibly small for this system. The results from Soejima et al [21] are somewhat higher than all other results and hardly vary over the given energy range, but are still with joint error bars. For N^{5+} and O^{6+} the situation is different: here the influence of ADC becomes more important. At an impact energy around 1 keV amu^{-1} the $q \rightarrow q-1$ cross sections are approximately 50% higher than our summed state-selective
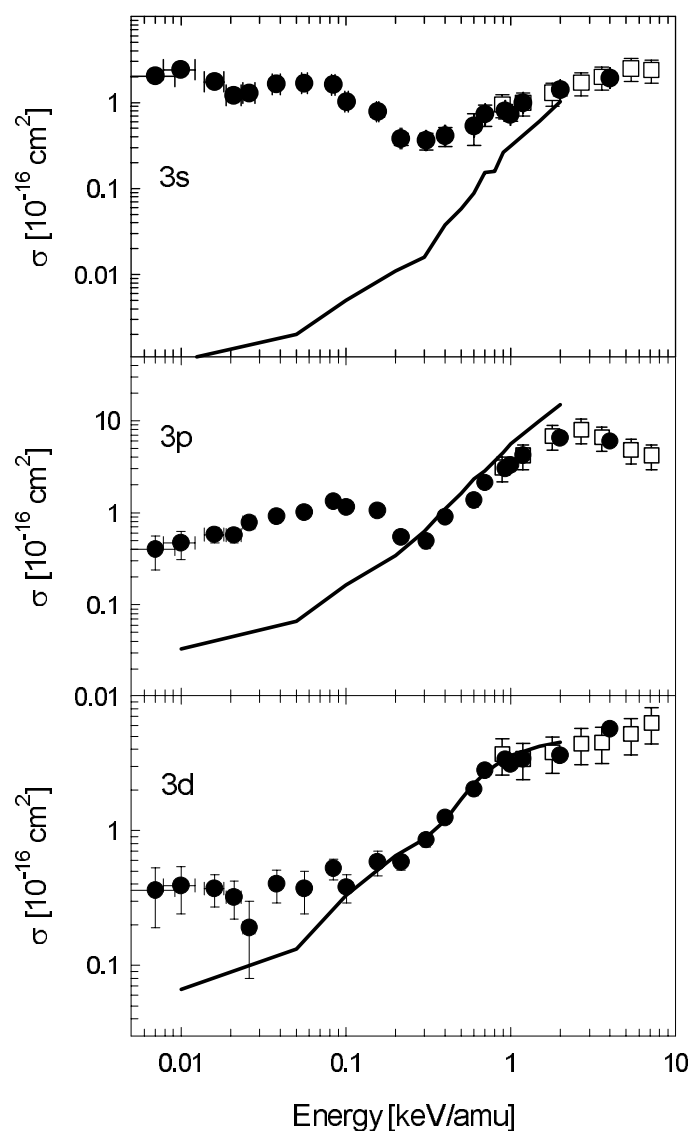
Figure 8. Comparison of our measured absolute state-selective cross sections for: ●, N^{5+} colliding on H_2; with □, experimental results of Dijkkamp et al [17]; and ——, theoretical calculations of Kumar and Saha [11].

ones. This difference matches cross sections for double-electron capture into autoionizing states [37].

3.2. Comparison with quantal and semi-quantal calculations

Regarding the system $C^{4+} + H_2$ there is good agreement between our results and the available calculations down to an impact energy of 100 eV amu^{-1}. At lower projectile energies we find deviations. In the energy range where ab initio calculations exist, our cross sections are well described by Errea et al [13], although they overestimate $\sigma(3p)$ by 20–40% above
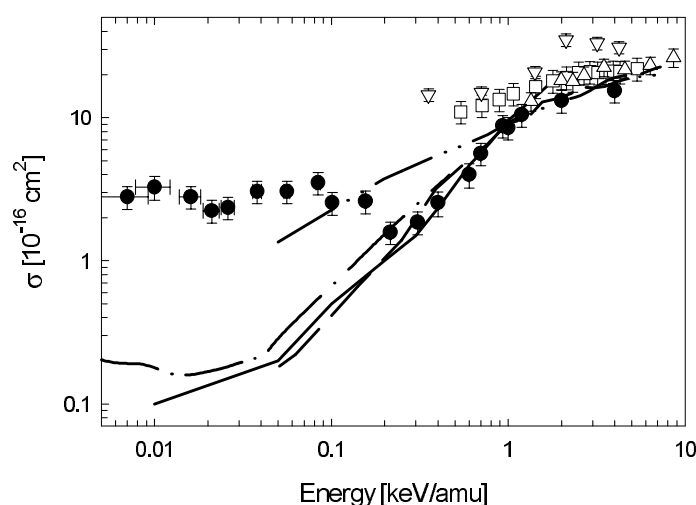
Figure 9. Total capture cross sections for $N^{5+} + H_2$. Theoretical results: $—\cdot—$, Gargaud and McCarroll [12]; $———$, Elizaga et al [14] and $—\cdot\cdot—$, [15]; $———$, Kumar and Saha [11] (summed cross sections for capture into $n = 3$). Experiments: $\triangle$, Crandall et al [18]; $\square$, Dijkkamp et al [17]; $\triangledown$, Panov et al [19]; $\bullet$, this work. The latter ones are the sums of the measured state-selective cross sections.

600 eV amu^{-1}. The calculations by Kumar and Saha [11] differ somewhat more from our results. They clearly overestimate $\sigma(3d)$ over the whole energy range as well as all substate cross sections above 500 eV amu^{-1} by approximately 50%. The strong increase of $\sigma(3s)$ and $\sigma(3p)$ predicted below 30 eV amu^{-1} is not in line with our measurements. The MO calculations by Gargaud and McCarroll [12] seem to describe the system fairly well, with the exception of $\sigma(3s)$, which below 50 eV amu^{-1} is clearly underestimated. The fact that the MO results of Gargaud and McCarroll give the best agreement is remarkable, since the least number of states (only Σ-states) was included.

The calculations by Kumar and Saha [11] for state-selective electron capture in collisions of N^{5+} and H_2 show a rather good agreement with our experimental results down to an impact energy of 200 eV amu^{-1}, although already at 1 keV amu^{-1} their $\sigma(3s)$ is significantly lower. From 200 eV amu^{-1} on down, large differences are found between their theoretical predictions and our measurements. This discrepancy is most pronounced for $\sigma(3s)$, where our results are several orders of magnitude higher. Comparing our summed partial cross sections (cf figure 9) with those of Kumar and Saha, Gargaud and McCarroll [12], and Elizaga et al [14], a similar situation is encountered. All theories agree well with our experiments down to 200 eV amu^{-1} projectile energy. From there on our measured cross section is slightly increasing again, whereas the theoretical values decrease strongly. This leads to a cross section which is of the order of 10 times lower than the experiments at the lowest impact energies. In a re-evaluation of their model calculations Elizaga et al [15] obtained results which are in better agreement with our measurements in the 50–150 eV amu^{-1} range. However, the new results overestimate the experimental data in the 200–800 eV amu^{-1} range.

In order to check for possible experimental artefacts we performed a number of tests. We measured the peak intensities shown in figure 12 for different target pressures at two different impact energies. Hereby we used one impact energy which was lower than the starting point of the increase in the cross section (see figure 9) and the undecelerated projectile beam, where the cross sections were found to be comparably higher. The figure shows that the linear regression
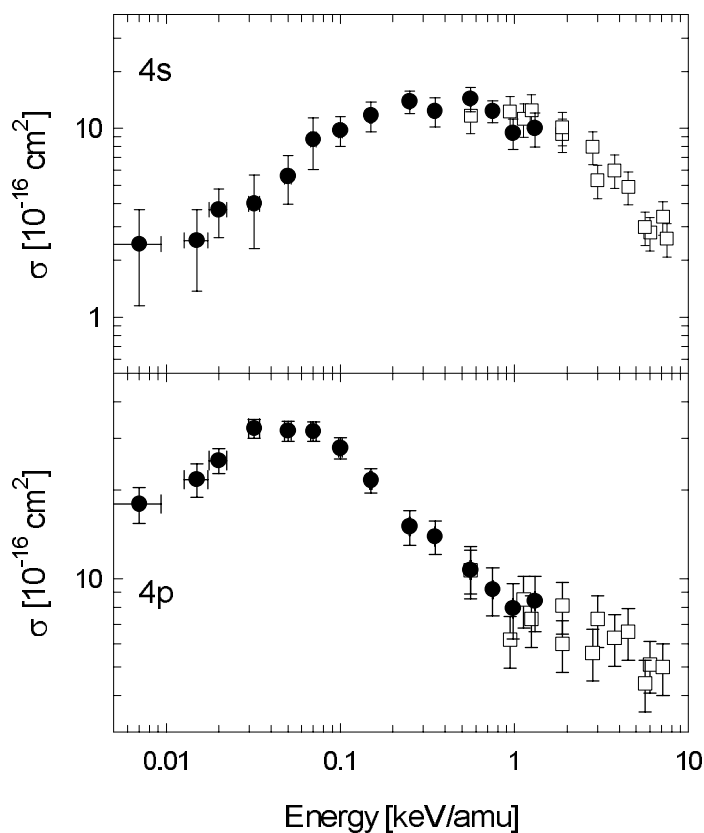
Figure 10. State-selective electron capture cross sections for the system $O^{6+} + H_2$. ●, this work; □, Dijkkamp et al [17].

in all cases includes the origin, which means with the target gas removed there is no detectable signal. Capture from the always present background gas is thus negligibly small. Secondly, the linear slope of the regression curve shows that the target density is kept low enough to ensure single ion–molecule collisions, i.e. the photon signals depend linearly on the target density for a certain cross section (cf equation (6)).

Comparing the cross sections obtained for a measurement with an uncooled nozzle and a cooled one no difference was found. Varying the RF power and frequency in the region of signal saturation (cf figure 4) yielded the same cross sections, indicating that the H_2 molecules are not dissociating due to the RF voltage on the octopole. This conclusion is further supported by the fact that capture into the $n = 4$ states vanishes completely towards lower impact energies, whereas these states are the predominantly populated ones for collisions of N^{5+} on atomic hydrogen [17].

For $O^{6+} + H_2$ no model calculations are available for comparison.

3.3. The dynamical over-barrier model

To explain the gross features of the various experimental results we use the dynamic [38] version of the over-barrier model. Within the framework of this model it is assumed that on their way to the collision the H_2 target electrons subsequently transit the potential-energy barrier
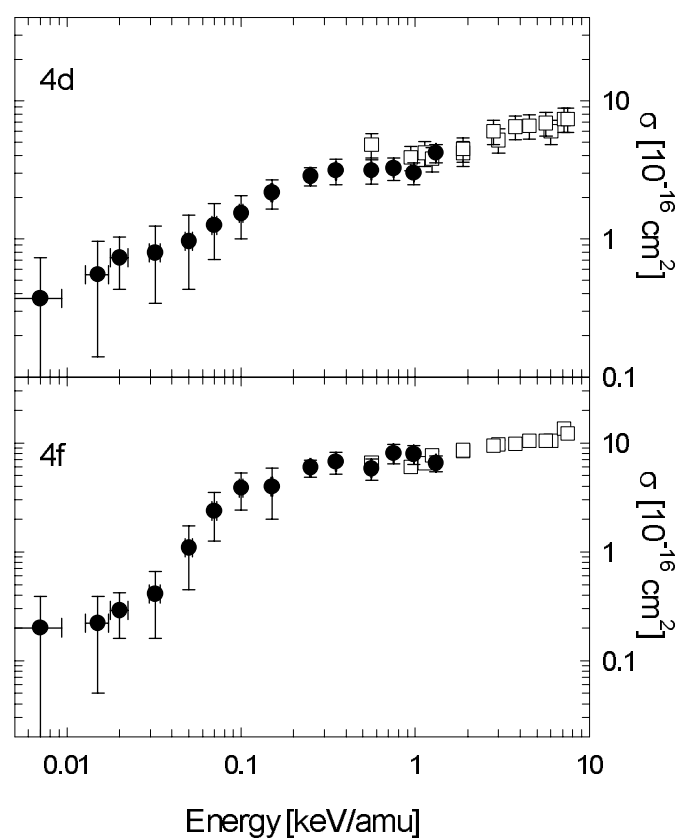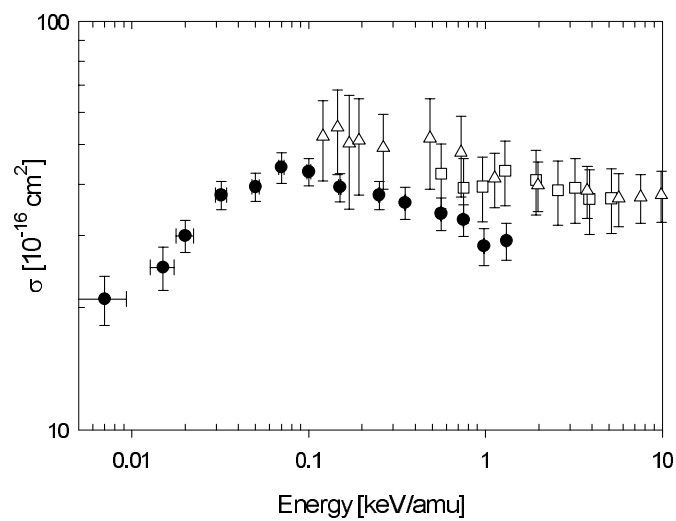
Figure 10. Continued.

Figure 11. Comparison of our summed partial cross sections (●) with the charge-changing cross sections by: △, Crandall et al [18] and □, Dijkkamp et al [17] for O^{6+} colliding on H_2.

Energy 85 eV/amu

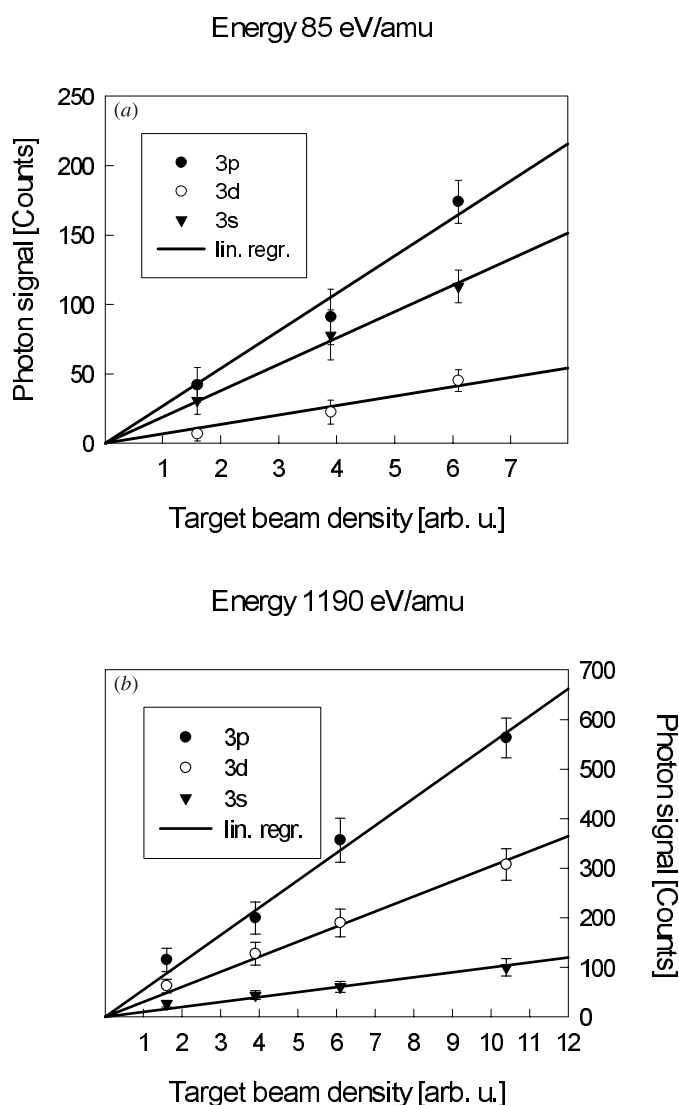(a)

Energy 1190 eV/amu

(b)

Figure 12. Measured photon signals from the $n = 3$ emission lines of N^{5+} versus the H_2 target pressure for an impact energy of (a) 85 eV amu^{-1} and (b) 1.19 keV amu^{-1}. The accumulated charge was the same in all measurements. The linear curves are included to guide the eye. The error bars represent statistical errors at the 90% confidence level.

between the molecule and the ion. The calculated capture distances R_1 and R_2 (for capture of the outer and inner electron, respectively), and corresponding geometrical cross sections, $\sigma_1 = \pi(R_1^2 - R_2^2)$ and $\sigma_2 = \pi R_2^2$ are given in table 6. After the transitions the electrons occupy transient molecular states within the joint potential-energy well of the collision partners. For impact parameters $R_2 \leqslant b \leqslant R_1$ only one electron becomes molecular, while for $b < R_2$ both electrons are active. The corresponding geometrical cross sections are, by accident, of similar magnitude. On the way out of the collision the electrons which became molecular, are redistributed over the projectile and the target. The electrons will populate states around the resonant transition energies. The population distributions, the so-called reaction windows

Table 6. Capture distances R_i and resulting geometrical cross sections σ_i for A^{q+} ions on H_2. Calculated are the capture of the outer electron ($i = 1$) and the inner one ($i = 2$), assuming an absorbing sphere model.

q	R_1 (au)	R_2 (au)	σ_1 (10^{-16} cm^2)	σ_2 (10^{-16} cm^2)
4	8.5	6.1	30.6	32.6
5	9.3	6.6	37.2	38.6
6	10.0	7.1	43.8	44.4

[38], for the observed systems together with the respective $4l$ and $3l$ energy levels in C IV, N V and O VI [30] are shown in figure 13. From the figure the main characteristics of the measured cross sections can be understood.

For C^{4+} projectiles the $4l$ levels are situated at a binding energy of approximately 14 eV in the far wing of the reaction window and hence they are only weakly populated. Even the $3l$ selective cross sections can be explained to some extent by the classical model. From the position of the $3l$ states with respect to the centre of the reaction window one would expect $\sigma(3p)$ and $\sigma(3s)$ to be of the same order of magnitude and $\sigma(3d)$ to be somewhat smaller. At low energies angular momentum arguments [39] amplify this trend: in the frame of an ion approaching the target with a velocity v the target electron has a classical angular momentum of the order of bv, where b is the impact parameter. For C^{4+} colliding on H_2, b ranges between 6.1 and 8.5 (cf table 6), leading to an angular momentum ranging between 0.27 and 0.38 for a projectile energy of 50 eV amu^{-1} ($v = 0.045$ au). Obviously, this value fits better to the s- than to the p- or d-states.

The position of the reaction window for $O^{6+} + H_2$ collisions indicates a predominant capture of the electrons into the $4l$ states since the $3l$ states at around 55–58 eV and the $5l$ states (around 20 eV, not shown in figure 13) lie outside the reaction window. This is indeed verified by our experimental results: exploiting formulae (14)–(16) we find that all the detected signals for the $3l \rightarrow 2l'$ transitions can be fully attributed to cascades out of the $n = 4$ levels. In detail, $\sigma(4f)$, in particular, is expected to become preferably populated, whereas the state population of $\sigma(4s)$ should decrease towards lower impact energies. In contrast our results show $\sigma(4f)$ to be significantly lower than $\sigma(4s)$. Angular momentum arguments [39] point in the right direction: for collisions of O^{6+} with H_2, b can reach a maximum value of 10.0 au and a minimum one of 7.1 au (cf table 6). The angular momentum for an impact energy of 50 eV amu^{-1} then ranges between 0.32 and 0.45, which fits apparently better to the s- than to the d- or f-state. Nevertheless, these arguments cannot explain the significant dominance of $\sigma(4p)$ at low projectile energies. Going to higher ion velocities the maximum of the angular momentum is shifted to higher values. At a projectile velocity of 1 keV amu^{-1} ($v = 0.2$ au) it becomes 2.2 and thus fits to the d- or f-state rather than to the s- and p-state. This can be seen in figure 10.

The cross sections for N^{5+} colliding with H_2 are expected to be rather small compared with those for C^{4+} and O^{6+}, because of the unfavourable position of the reaction window in the gap between $n = 3$ and 4 shells. Indeed, total one-electron capture cross sections for collisions of N^{5+} on H_2 are approximately one order of magnitude smaller than those for C^{4+} and O^{6+} projectiles. For such small cross sections other contributions have to be considered, e.g. two-electron processes ($b < 6.6$) for which it is found that the strongest bound electron can near-resonantly populate the $N^{4+}(3s)$ state, while recapture of the loosely bound electron by the hydrogen target is resonant with the ground state of the H_2^+ molecule [40]. In this way two-electron processes lead to one-electron capture. Only a small fraction (5–10%) of the geometrical cross section for two-electron processes is already enough to explain the measured
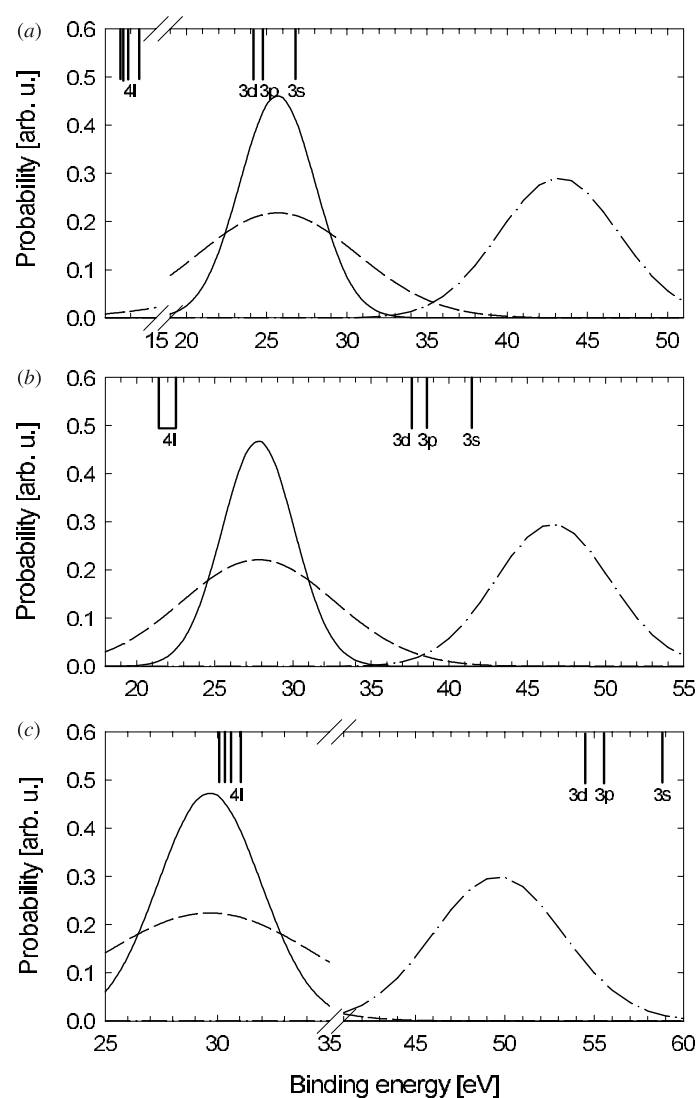
Figure 13. Reaction windows [38] for electron capture in collisions of (a) C^{4+}, (b) N^{5+} and (c) O^{6+} with H_2, respectively. Shown are the capture probabilities for capture of the outer electron (——, 50 eV amu^{-1}; – – –, 1 keV amu^{-1}) together with those for the inner electron (— · —, 50 eV amu^{-1}).

one-electron capture cross sections. Since from these considerations the importance of two-electron processes becomes clear, we propose that models should include these processes in the calculation of one-electron capture cross sections.

4. Conclusion

In conclusion, we have brought into operation a combined RF-guided ion beam and photon emission spectroscopy method to measure state-selective charge-transfer cross sections at energies of direct relevance for astrophysics and fusion-plasma diagnostics and modelling. As

examples the He-like systems C^{4+}, N^{5+} and O^{6+} colliding on H_2 have been discussed. The ion energy has been varied down to energies as low as 5 eV amu^{-1}. In combination with a recoil ion source, the energies might be lowered much further. The excellent agreement of our results for state-selective one-electron capture cross sections with all other available experimental data confirms that with the technique described in this paper we are able to perform results over a wide range of impact energies. Unexpectedly large differences (orders of magnitude!) with theory have been observed, implying that the present and future measurements are valuable as benchmarks for improving theoretical descriptions

Acknowledgments

References

[1] Isler R C 1994 Plasma Phys. Control. Fusion 36 171
[2] Anderson H, von Hellermann M, Hoekstra R, Horton L D, Howman A C, Konig R W T, Martin R, Olson R E and Summers H P 2000 Plasma Phys. Control. Fusion 42 781
[3] Kingdon J B and Ferland G J 1999 Astrophys. J. 516 L107
[4] Lisse C M et al 1996 Science 274 205
[5] Häberli R M, Gombosi T I, de Zeeuw D L, Combi M R and Powell K G 1997 Science 276 939
[6] Krasnopolsky V A, Mumma M J, Abbott M, Flynn B C, Meech K J, Yeomans D K, Feldman P D and Cosmovici C B 1997 Science 277 1488
[7] Lisse C M, Christian D, Dennerl K, Englhauser J, Trumper J, Desch M, Marshall F E, Petre R and Snowden S 1999 Icarus 141 316
[8] Luhmann J 2000 Phys. World 13 31
[9] Kamber E Y and Ferguson S M 1999 Phys. Scr. T 80 359
[10] Akgüngör K, Kamber E Y and Ferguson S M 1999 Rapid Commun. Mass Spectrom. 13 412
[11] Kumar A and Saha B C 1999 Phys. Rev. A 59 1273
[12] Gargaud M and McCarroll R 1985 J. Phys. B: At. Mol. Phys. 18 463
[13] Errea L F, Gorfinkiel J D, Macías A, Méndez L and Riera A 1999 J. Phys. B: At. Mol. Opt. Phys. 32 1705
[14] Elizaga D, Errea L F, Macías A, Méndez L, Riera A and Rojas A 1999 Phys. Scr. T 80 187
[15] Elizaga D, Errea L F, Gorfinkiel J D, Illescas C, Macías A, Méndez L, Rabadan I, Riera A, Rojas A and Sanz P to be published
[16] Fritsch W 1992 Phys. Rev. A 46 3910
[17] Dijkkamp D, Ćirić D, Vlieg E, de Boer A and de Heer F J 1985 J. Phys. B: At. Mol. Phys. 18 4763
[18] Crandall D H, Phaneuf R A and Meyer F W 1979 Phys. Rev. A 19 504
[19] Panov M N, Basalaev A A and Lozhkin K O 1983 Phys. Scr. T 3 124
[20] Hoekstra R, Beijers J P M, Schlatman A R and Morgenstern R 1990 Phys. Rev. A 41 4800
[21] Soejima K, Latimer C J, Okuno K, Kobayashi N and Kaneko Y 1992 J. Phys. B: At. Mol. Opt. Phys. 25 3009
[22] Cocke C L and Olson R E 1991 Phys. Rep. 205 153
[23] Teloy E and Gerlich D 1974 Chem. Phys. 4 417
[24] Gerlich D 1992 Adv. Chem. Phys. 82 1
[25] Okuno K, Soejima K and Kaneko Y 1991 Nucl. Instrum. Methods B 53 387
[26] Bliek F W, Woestenenk G R, Hoekstra R and Morgenstern R 1997 Hyperfine Interact. 108 121
[27] Dahl D A 1990 Simion 3D Version 6.0 Idaho National Engineering Laboratory, ID
[28] Hoekstra R, de Heer F J and Morgenstern R 1991 J. Phys. B: At. Mol. Opt. Phys. 24 4025
[29] Hoekstra R, Folkerts H O, Beijers J P M, Morgenstern R and de Heer F J 1994 J. Phys. B: At. Mol. Opt. Phys. 27 2021
[30] Bashkin S and Stoner J O 1975 Atomic Energy Levels and Grotrian Diagrams (Amsterdam: North-Holland)

[31] Lindgard A and Nielsen S E 1977 At. Nucl. Data Tables **19** 533
[32] Cocke C L 1976 Methods of Experimental Physics: Spectroscopy vol 13, ed D Williams (New York: Academic) pp 256–72
[33] Marrus R 1973 Nucl. Instrum. Methods **110** 333
[34] Richard P 1975 Atomic Inner Shell Processes ed B Crasemann (New York: Academic) pp 140–59
[35] Sellin I A 1976 Advances in Atomic and Molecular Physics vol 12, ed D R Bates and B Bederson (New York: Academic) pp 215–80
[36] Mack E M 1987 PhD Thesis Rijksuniversiteit Utrecht
[37] Bordenave-Montesquieu A, Boudjema M, Benoit-Cattin P, Gleizes A and Moretto-Capelle P 1989 J. Phys. Colloq. **50** 305
[38] Niehaus A 1986 J. Phys. B: At. Mol. Phys. **19** 2925
[39] Burgdörfer J, Morgenstern R and Niehaus A 1987 Nucl. Instrum. Methods B **23** 120
[40] Steinfeld J I 1974 Molecules and Radiation: an Introduction to Modern Molecular Spectroscopy (New York: Harper and Row)
[41] Drake G W F, Victor G A and Dalgarno A 1969 Phys. Rev. **180** 25
[42] Druetta M, Martin S and Desesquelles J 1987 Nucl. Instrum. Methods B **23** 268
[43] Snowdon K J, Havener C C, Meyer F W, Overbury S, Zehner D M and Heiland W 1988 Rev. Sci. Instrum. **59** 902